2014-10

MEMS-Scale Turbomachinery Based Vacuum Roughing Pump

Gannon, Anthony J.; Hobson, Garth V.; Shea, Michael J.; Clay, Christopher S.; Millsaps, Knox T.

The American Society of Mechanical Engineers (ASME)

Gannon, Anthony J., et al. "MEMS-scale turbomachinery based vacuum roughing pump." Journal of Turbomachinery 136.10 (2014): 101002.
http://hdl.handle.net/10945/62498

Anthony J. Gannon
MAE Department,
Naval Postgraduate School,
700 Dyer Road, Room 245,
Monterey, CA 93943
e-mail: ajgannon@nps.edu

Garth V. Hobson
MAE Department,
Naval Postgraduate School,
700 Dyer Road, Room 245,
Monterey, CA 93943
e-mail: gvhobson@nps.edu

Michael J. Shea
MAE Department,
Naval Postgraduate School,
700 Dyer Road, Room 245,
Monterey, CA 93943
e-mail: michaelshea2011@gmail.com

Christopher S. Clay
MAE Department,
Naval Postgraduate School,
700 Dyer Road, Room 245,
Monterey, CA 93943
e-mail: clayoven2@yahoo.com

Knox T. Millsaps
MAE Department,
Naval Postgraduate School,
700 Dyer Road, Room 245,
Monterey, CA 93943
e-mail: millsaps@nps.edu

MEMS-Scale Turbomachinery Based Vacuum Roughing Pump

This study forms part of a program to develop a micro-electro-mechanical systems (MEMS) scale turbomachinery based vacuum pump and investigates the roughing portion of such a system. Such a machine would have many radial stages with the exhaust stages operating near atmospheric conditions while the inlet stages operate at near vacuum conditions. In low vacuum such as those to the inlet of a roughing pump, the flow can still be treated as a continuum; however, the no-slip boundary condition is not accurate. The Knudsen number becomes a dominant nondimensional parameter in these machines due to their small size and low pressures. As the Knudsen number increases, slip-flow becomes present at the walls. The study begins with a basic overview on implementing the slip wall boundary condition in a commercial code by specifying the wall shear stress based on the mean-free-path of the gas molecules. This is validated against an available micro-Poiseuille classical solution at Knudsen numbers between 0.001 and 0.1 with reasonable agreement found. The method of specifying the wall shear stress is then applied to a generic MEMS scale roughing pump stage that consists of two stators and a rotor operating at a nominal absolute pressure of 500 Pa. The zero flow case was simulated in all cases as the pump down time for these machines is small due to the small volume being evacuated. Initial transient two-dimensional (2D) simulations are used to evaluate three boundary conditions, classical no-slip, specified-shear, and slip-flow. It is found that the stage pressure rise increased as the flow began to slip at the walls. In addition, it was found that at lower pressures the pure slip boundary condition resulted in very similar predictions to the specified-shear simulations. As the specified-shear simulations are computationally expensive it is reasonable to use slip-flow boundary conditions. This approach was used to perform three-dimensional (3D) simulations of the stage. Again the stage pressure increased when slip-flow was present compared with the classical no-slip boundaries. A characteristic of MEMS scale turbomachinery are the large relative tip gaps requiring 3D simulations. A tip gap sensitivity study was performed and it was found that when no-slip boundaries were present the pressure ratio increased significantly with decreasing tip gap. When slip-flow boundaries were present, this relationship was far weaker. [DOI: 10.1115/1.4027971]

Introduction

MEMS scale pumps have potential applications in sensing and medical devices where vacuums are required. At present, the generation of a suitable vacuum is performed by generally large machinery and requires high power levels to drive it. MEMS scale devices have the potential to put many stages on a single rotor to achieve the required vacuum at a low power level and in a small scale device. By making the devices smaller, more stages can be placed on a single rotor disk and rotated at a lower speed to achieve the same pressure ratio while having the advantage of decreased power usage. There is the potential to have handheld devices capable of producing high vacuums. A further advantage of turbomachinery vacuum pumps over positive displacement pumps is their fast pump down time due to their high volume flow-rate capabilities.

It must be noted that the photolithography based manufacturing process for MEMS devices results in 2D blade shapes with no twist is possible. This constraint is offset by the extreme miniaturization made possible by the process and the ability to easily produce multiple stages on a single wafer. The best solution for these 2D blade shapes is a radial type device with interlocking rotors and stators. Figure 1 shows a cross sectional layout for such a device. In a real device, the stages would be far smaller and many more would be able to be manufactured on a single wafer. The layout of the device is also important so that no part of the bearings and associated lubrication system is exposed to the vacuum. While MEMS scale turbomachinery for gas turbine applications have been widely investigated with an overview given by Lang [1], their use for vacuum applications is fairly new.

Vacuum systems usually consist of two types of pumps in series. The first produces is connected the very high vacuum section and typically exhausts to a pressure between 1 and 2 Pa. The second pump, called a roughing pump operates between the high vacuum pump exhaust and atmospheric pressure. A good overview of vacuum technology is given by Rozanov [2]. The current study looks at a stage suitable for a roughing pump. First, an

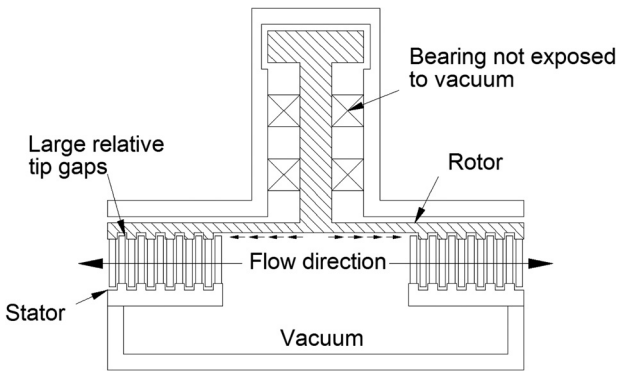

Fig. 1 MEMS scale vacuum or roughing pump

Contributed by the International Gas Turbine Institute (IGTI) of ASME for publication in the JOURNAL OF TURBOMACHINERY. Manuscript received May 30, 2014; final manuscript received June 5, 2014; published online July 15, 2014. Editor: Ronald Bunker.

Table 1 Knudsen number regimes

Navier–Stokes equations with no-slip boundary conditions	$\mathrm{Kn} < 10^{-3}$
Navier–Stokes equations with slip boundary conditions	$10^{-3} \leq \mathrm{Kn} < 10^{-1}$
Transition regime	$10^{-1} \leq \mathrm{Kn} < 10$
Free-molecular flow	$\mathrm{Kn} \geq 10$

Table 2 ANSYS CFX user expression code

MolecularDiam = 3.7×10^{-10} (m)
MeanFreePath = Boltzmann × Temperature/(sqrt(2) × pi × Absolute Pressure × MolecularDiam^2)
ShearSlip x = −Velocity u × Dynamic Viscosity/MeanFreePath
ShearSlip y = −Velocity v × Dynamic Viscosity/MeanFreePath
ShearSlip z = −Velocity w × Dynamic Viscosity/MeanFreePath

investigation into the modifications required to simulate low pressure near vacuum flow is undertaken. Following this, a 2D simulation is performed to determine a suitable blade shape for the stage that can be manufactured. Finally, a 3D simulation is performed to investigate the effects of the large relative tip gaps found in these types of devices.

Low Pressure MEMS Scale Flows

In flows where the characteristic length scale L is of a similar magnitude to the mean-free-path of the gas molecules $\mathcal{L}$, the Knudsen number Kn, which is the ratio of these two becomes an important parameter

$$\mathrm{Kn} = \frac{\mathcal{L}}{L} \tag{1}$$

Gad-el-Hak [3] gives an overview of the relevant Knudsen number scales and the solution techniques required to solve each. These are summarized in Table 1. For most turbomachinery flows this ratio is near-zero. When the Knudsen number becomes larger, the no-slip boundary condition typically used at walls is no longer accurate and the flow on the wall surface begins to have a finite nonzero velocity. This is due to the noncontinuum effects of individual gas molecules. For $0.001 < \mathrm{Kn} < 0.1$, the continuum Navier–Stokes equations may still be used to simulate the flow but require a slip boundary condition as noted in Table 1. In MEMS scale turbomachinery operating at low pressures, the Knudsen number is large enough that there will be appreciable slip between the fluid and the boundary walls. This is the regime that the roughing pump stage investigated in this study is expected to operate in.

Barber and Emerson [4] give a concise summary of the boundary conditions required to simulate slip-flows of $\mathrm{Kn} \approx 0.1$. Applying the slip boundary condition begins with calculating the mean-free-path of the gas molecules $\mathcal{L}$ using Eq. (2). It assumes an ideal gas with the molecules modeled as rigid spheres, where k is the Boltzmann constant, T the temperature, p the pressure, and σ the molecular diameter

$$\mathcal{L} = \frac{kT}{\sqrt{2}\pi p \sigma_c^2} \tag{2}$$

In order to simulate a slip-flow, the wall shear stress τ must be specified directly. A first order expression for tangential slip velocity u_t, first proposed by Basset [5] is shown in Eq. (3), where σ_v is the tangential-momentum-accommodation coefficient, which is 0 for perfectly smooth walls where molecules conserve their tangential momentum and 1 for extremely rough wall where they lose all their tangential momentum

$$u_t = \frac{2 - \sigma_v}{\sigma_v} \mathcal{L} \frac{\partial u}{\partial y} \tag{3}$$

A conservative approach assuming $\sigma_v = 1$ is used as the process of photolithography sometimes produces rough walls especially as the machine sizes decrease. This simplifies the tangential slip velocity equation to

$$u_t = \mathcal{L} \frac{\partial u}{\partial y} \tag{4}$$

The velocity gradient is dependent on the shear τ at the wall

$$\tau = \mu \frac{\partial u}{\partial y} \tag{5}$$

Substitution leads to the tangential slip velocity being defined in terms of the mean-free-path $\mathcal{L}$, wall shear τ, and the fluid dynamic viscosity μ.

$$u_t = \mathcal{L} \frac{\tau}{\mu} \tag{6}$$

Rearranging the wall shear stress can then be specified

$$\tau = u_t \frac{\mu}{\mathcal{L}} \tag{7}$$

Slip Velocity Simulation. It can be seen from Eq. (7) that the wall shear stress is a function of the slip velocity meaning that an iterative solution to the problem is required. The commercial package ANSYS CFX was used for all simulation presented in this study. User expressions were implemented to allow for slip-flows at the wall with the code shown in Table 2.

The molecular diameter (MolecularDiam) is the mean for air [1]. MeanFreePath is an implementation of Eq. (2) while ShearSlip $x/y/z$ are implementations of Eq. (7) for each Cartesian component. Use of the expressions proved to be robust in various test cases as well as in 2D simulations of the actual compressor stages. There was a high computational overhead for 3D simulations due to the iterative nature of the solution.

Numerical instabilities would occur at higher absolute pressures if slip-flow was still assumed. The mean-free-path of the molecules decreases at higher pressures, which would lead to a calculated wall shear with a value actually higher than for the no-slip case. While a more robust implementation of the expressions may be possible, the cases simulated in this study were all in the no-slip region with nominal pressure of 500 Pa used.

Laminar Flow Assumption. A Reynolds number, Eq. (8), based on any length scale L, within a MEMS device operating at low pressure and thus low densities will be small. Due to this, it is reasonable to assume that the flow will be laminar

$$\mathrm{Re} = \frac{\rho u L}{\mu} \tag{8}$$

Poiseuille Flow Test Case. To investigate the performance of the simulation using a specified-shear stress at the boundary a pressure driven micro-Poiseuille flow was simulated. Figure 2 shows the simulated 2D control volume. A grid independence study was performed, and no change to the result was found from further refinement of the mesh. The solutions were converged to machine precision. Liou and Fang [6] provide an analytical solution for micro-Poiseuille flows with slip boundary conditions. Assuming adiabatic walls (a good approximation for silicone at ambient temperatures), the parabolic velocity profile, that is, the solution to the classical Poiseuille flow remains the same but is offset by the slip velocity at the wall. Figure 3 shows the

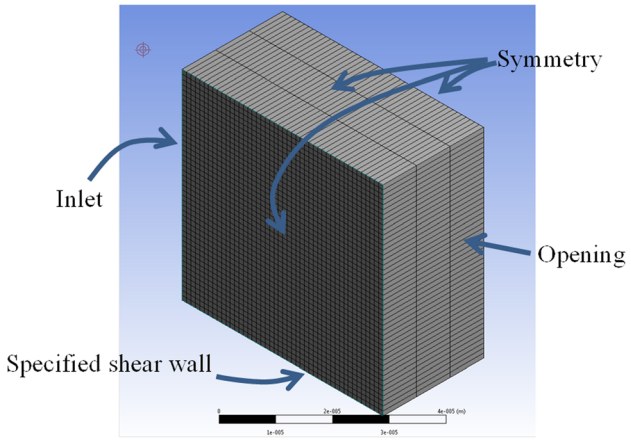

Fig. 2 Boundary conditions for Poiseuille simulation

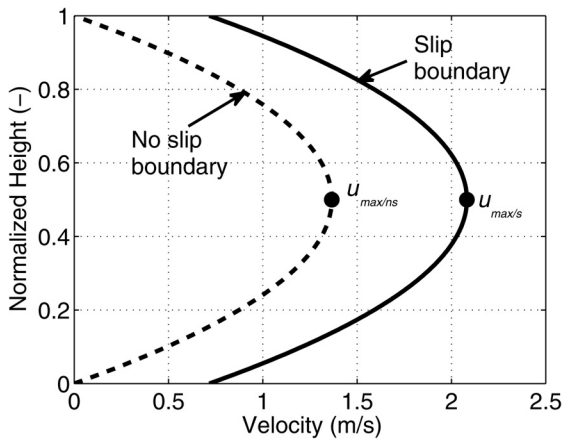

Fig. 3 Poiseuille velocity profile comparison

comparison between velocity profiles for the slip and no-slip boundary conditions. The maximum velocities for the no-slip and slip boundary conditions are $u_{max/ns}$ and $u_{max/s}$, respectively.

Table 3 shows four of the Poiseuille test cases simulated. The bolded data row corresponds to the velocity profiles shown in Fig. 3. To vary the Knudsen number, the channel height L was increased (Eq. (1)). Decreasing the pressure p increases the mean-free-path of the gas molecules $\mathcal{L}$ in Eq. (2), which also decreases the Knudsen number. For the lowest simulated Knudsen number of 0.033, the pressure gradient was reduced to -0.002 Pa/μm to limit the velocities.

Liou and Fang [6] show that for very rough walls ($\sigma_v = 1$), the maximum velocities are related to the Knudsen number by the following equation:

$$\frac{(u_{max/ns} - u_{max/s})}{u_{max/ns}} = 4\,\mathrm{Kn} \tag{9}$$

Figure 4 compares the simulated data with the classical solution [4]. There is a slight deviation at higher Knudsen numbers, but overall, the agreement is good.

Rotor Design

As mentioned, the blade designs are constrained to 2D shapes by the photolithography manufacturing process. The blade and stage sizes produced in the current study are large for MEMS devices, but to allow for smaller scale devices in future iterations, the blade shapes are kept to simple polygons. For vacuum pumps,

Table 3 Poiseuille slip versus no-slip comparisons

Kn	L (μm)	p (Pa)	dp (Pa/μm)	$u_{max/ns}$ (m/s)	$u_{max/s}$ (m/s)
0.033	1000	200	−0.002	13.55	15.32
0.044	500	300	−0.02	33.54	39.28
0.131	100	500	−0.02	1.374	2.082
0.164	100	400	−0.02	1.374	2.262

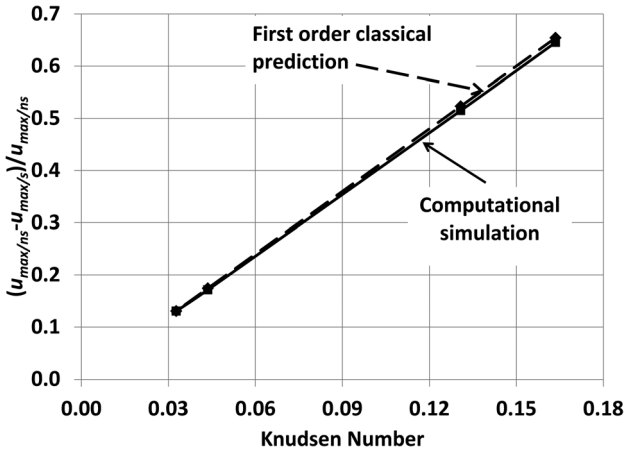

Fig. 4 Comparison of theory and simulation

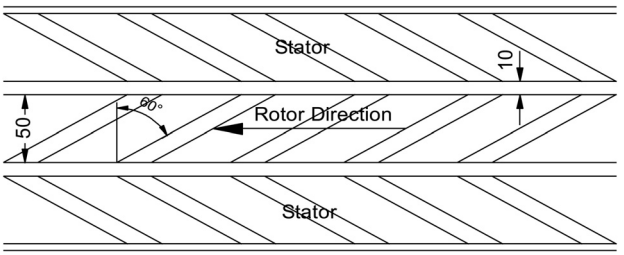

Fig. 5 Rotor and stator blade shapes (dimensions in μm)

the main requirement is to have a maximum pressure ratio. While some pumping occurs during the initial phase of operation the compressor operates at a near-zero flow-rate. This simplifies the design process as the machine requires optimization at a single point rather than over a large flow range. Figure 5 shows a cross section of the simple blade sections used. The stages are repeating with the rotor and stator being identical.

While manufacture of the rotor and stator to micron tolerances is possible the assembly of the rotor and stator is more difficult. This requires allowance for large tip gaps and interstage rotor/stator gaps when compared to the blade height and width. Table 4 outlines the rotor geometry and design speeds and corresponds to the dimensions shown in Fig. 5. The blade thickness was limited by the manufacturing tolerance and strength requirements of the blade. It is foreseen that the blade sizes will reduce allowing more stages to be packed onto a single disk in future. Test rotors have been run at speeds higher than 100,000 rpm, and stress is not an issue due to the very small diameters of the machine.

A lower speed machine with more stages is preferable in this type of device as it reduces the power consumption. The tip speed of the outer stage is 83.6 m/s, which means the flow in an individual stage can be treated as incompressible. Due to the ability to pack many stages onto a single wafer the overall pressure ratio is high. Figure 6 shows a single etched blade row while complete rotors and stators will have multiple blade rows.

Table 4 Rotor details

Blade height	150 μm	Blade thickness	12 μm
Nominal tip gap	10 μm	Pedestal height	20 μm
Radial blade size	50 μm	Blade row gap	10 μm
Blade stagger	60 deg	Outer diameter	16 mm
Design speed	100 krpm	Tip speed	83.8 m/s
Simulated speed	1000 rpm	Blade number	1000

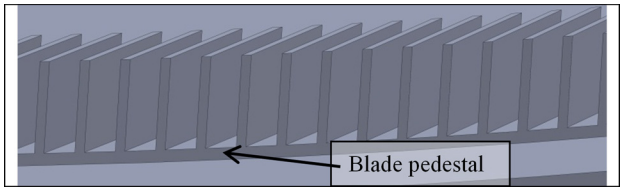

Fig. 6 Final etched blade shapes

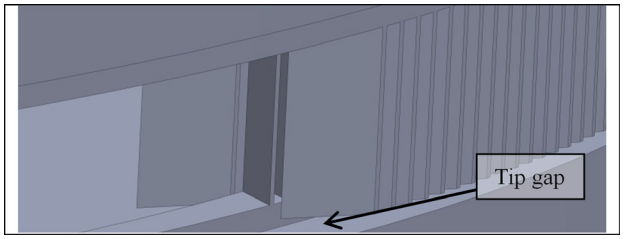

Fig. 7 Rotor and stator stage assembly

Figure 7 shows an assembled rotor blade with two surrounding stator blade rows. The interlocking arrangement that the pedestal allows can be seen. This interlocking arrangement creates a more difficult path for the leakage flow to follow, which counters the effects of the large tip gaps.

2D Rotor Simulation

As a first step in the design and analysis process, 2D rotor simulations are performed. Initial attempts performing the simulations at the design speed of 100,000 rpm using compressible flow were not successful. Even using very small time steps and running the solutions to machine precision did not give stable solutions. Switching to a slower rotation of 1000 rpm and using an incompressible solver allowed the specified-shear simulation to be used. It was necessary to initialize the problem by slowly increasing the rotational speed in steps from 0, 10, 100, and finally 1000 rpm. While this is below the design speed, the flows in both the simulation at 1000 rpm and operation at 100,000 rpm are incompressible.

Figure 8 shows a coarse version of the 2D mesh used. As mentioned, the vacuum pump application of this compressor meant that except for the initial pump down period the compressor was operating in a near-zero flow-rate environment. This meant that the interaction between the blade rows was great and coupled with the physically close blade spacing of MEMS devices, transient simulations were required. Some attempts were made using steady-state simulations using interface averaging, but these resulted in physically unrealistic solutions. The computational expense of these transient simulations requires the use of the 2D simulations for blade design. They allow fairly rapid investigations of overall blade geometry changes.

The blades angles and number presented are a crudely optimized shape to give the maximum pressure ratio for a zero flow-rate case. The result of this optimization leads to a blade stagger angle and blade number of 60 deg and 1000, respectively, for the outermost stage. Increases to the stagger angle or the blade number decreased the zero flow-rate pressure rise.

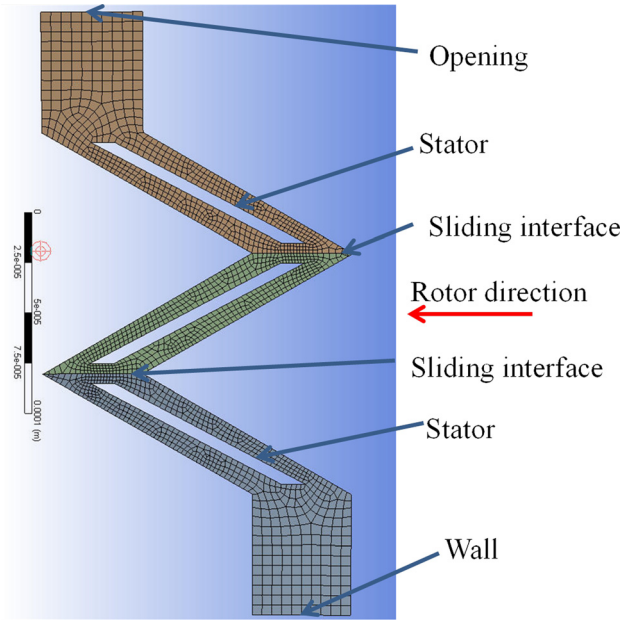

Fig. 8 2D simulation mesh

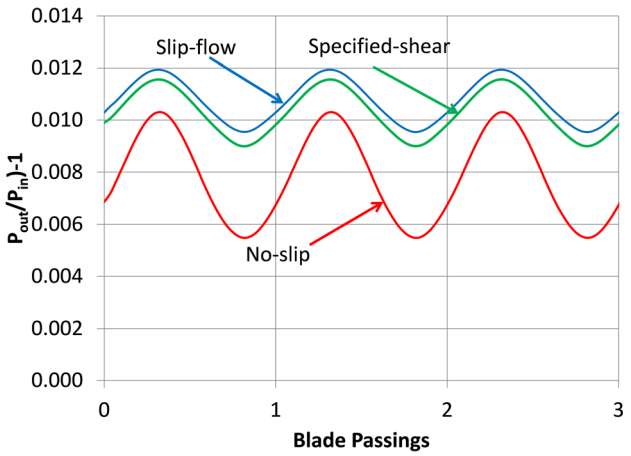

Fig. 9 Effect of wall boundary on pressure ratio (2D)

As before, a grid independence study was performed, and the results from the fine grid are presented in Fig. 9. The graph shows the pressure ratio across a single rotor surrounded by stators with unity subtracted for clarity. Of interest is the fact that when the flow is not subject to the classical no-slip boundary condition the pressure rise actually increases. A third simulation using a pure slip boundary condition was also performed. It can be seen that the difference between the specified-shear and the slip boundary condition is actually very small for the zero net flow simulation. Thus, it is a good approximation and computationally far less expensive to run the slip boundary condition. This simplification is used to investigate the effects of tip gaps described later. A further effect of the wall boundary condition is the reduction in amplitude of the pressure ratio for the specified-shear and slip-flow boundary conditions. Presumably this is due to a lessening of the effect of the relative motion between blade rows. The slip boundary conditions will lessen the velocity gradients between blade rows.

Figures 10 and 11 show the vortex flows that are set up at the blade leading and trailing edges for the no-slip and specified-shear flow cases, respectively. It was found that sharp leading edges gave the best performance for this type of application. The high pressure stagnation region caused at a blunt leading edge

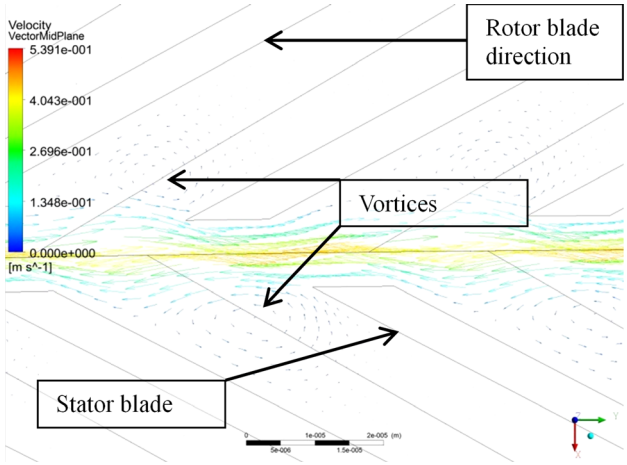

Fig. 10 Classical no-slip boundary condition

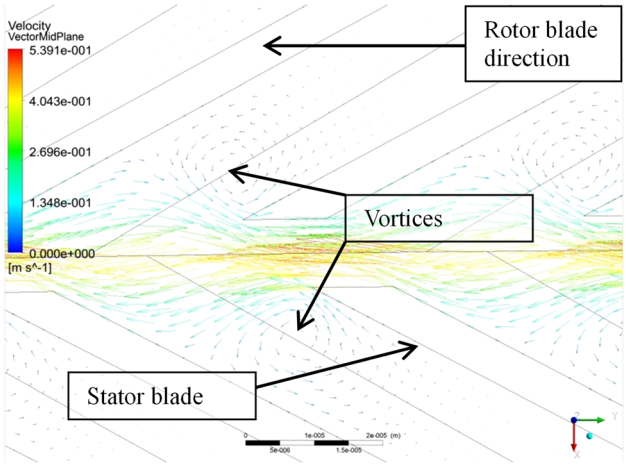

Fig. 11 Specified-shear boundary condition

reduces the zero flow pressure ratio. The scaling of the vectors is the same for both figures, and so, it can be clearly seen that the no-slip boundary condition results in weaker vortices than for the specified-shear boundary conditions. The interstage velocities are also higher in the specified-shear case. The transient simulation also shows that the flow within the blade passage eventually settles in an oscillating pattern for the near-zero flow-rate condition.

The enlarged vortices and higher interstage velocities may account for the higher pressure ratio for the specified-shear and slip-flow cases. The stagnation pressures at the interstage boundaries are high when slip is present. Figures 12 and 13 show the pressure contours for the no-slip and specified-shear flow cases, respectively. This is again at the near-zero flow-rate condition with the pressure scales being the same on both figures. It can be seen that the no-slip boundary condition does not lower the pressure at the stage inlet as much as for the specified-shear case. The work done by the rotor does heat the gas, but as these devices run for very short durations, this has not been an issue during operation. The simulations here assume nonconducting walls implying no machine heat removal and at 1000 rpm the temperature increase was 0.2 K.

3D Rotor Simulation

As mentioned, an issue with the turbomachine being investigated here is the large relative tip gap due to the constraints of assembling these devices. It is therefore not sufficient to rely on the 2D simulations of the stage but 3D simulations must be performed

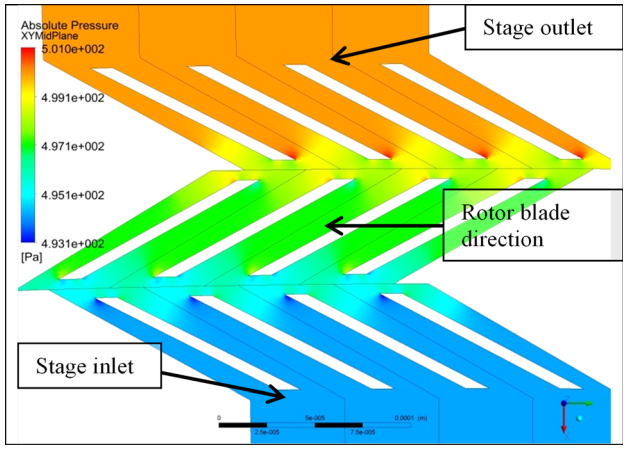

Fig. 12 2D simulation pressure contours: no-slip walls

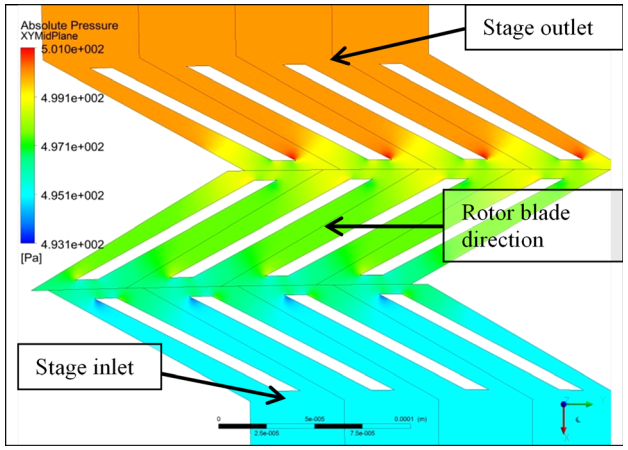

Fig. 13 2D simulation pressure contours: specified-shear

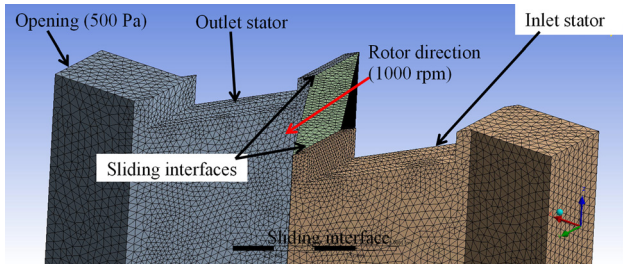

Fig. 14 3D simulation mesh

that include the tip gap region. Figure 7 shows the stage simulated while Fig. 14 shows a coarse mesh representation of the problem. A finer mesh was used in the actual simulations. The pedestals and tip gaps are included and the 3D simulations are performed at the same operating conditions as the 2D. For the initial simulations, a 10 μm tip gap was used. This meant that the blade tip was captured at the half way point of the 20 μm blade pedestal.

As mentioned earlier, the specified-shear condition added considerably to the computational load, and from Fig. 9, it can be seen that almost identical results to the slip boundary condition were obtained. For this reason, it was decided to use the slip boundary condition only to replicate low pressure flows in the 3D simulations. This also resulted in far more stable simulations with larger time steps and faster numerical rotor accelerations being possible. A typical solution took a day using six cores on a

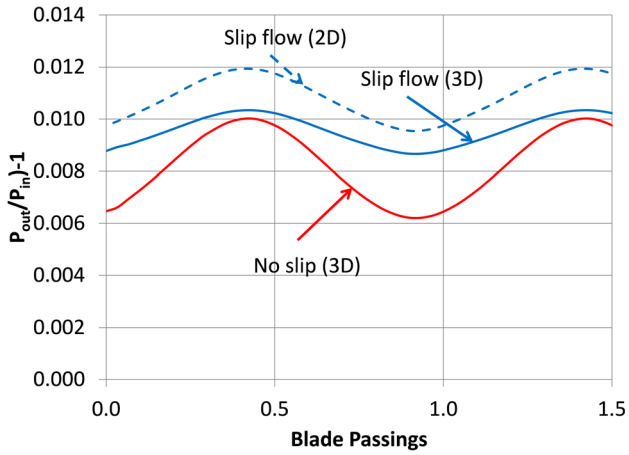

Fig. 15 Effect of wall boundary on pressure ratio (3D)

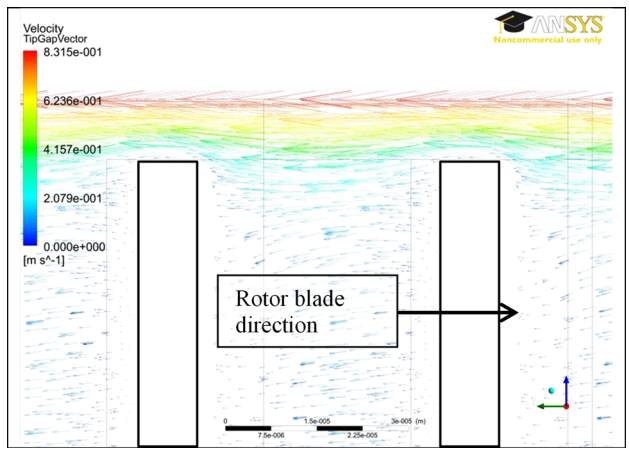

Fig. 16 Tip gap flow for no-slip boundary condition

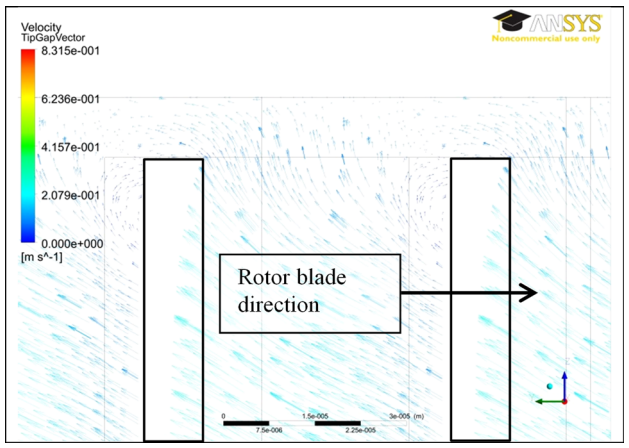

Fig. 17 Tip gap flow for slip boundary condition

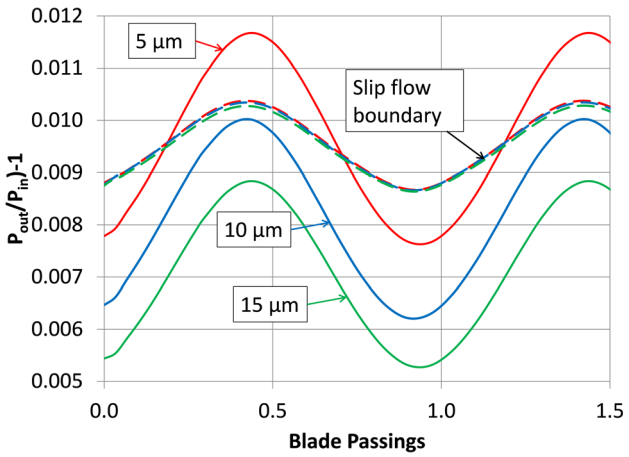

Fig. 18 Effect of tip gap on pressure ratio no-slip flow

personal computer. Figure 15 shows the difference in pressure ratios between the no-slip and slip boundary conditions. As with the 2D case, the slip-flow boundary conditions result in a higher pressure ratio over the stage. The variation in pressure rise is less with each blade passing for the no-slip case. Also included is the 2D slip boundary simulation. The pressure ratio can be seen to be higher due to there being no tip leakage.

Figures 16 and 17 show rotor velocity vector fields in the relative frame for the no-slip and slip-flow boundary conditions, respectively. The plane shown is in the tip region near the rotor blade exit with the same scale common to both figures. The no-slip stationary wall above the rotor tip results in a large velocity gradient between the rotor and wall and is typical of turbomachinery tip gap flows. When the pressure drops and the Knudsen number increases, slip-flow begins and the flow in the tip region begins to be entrained with the rotor. This results in lower losses and increases the pressure rise of the stage.

Tip Gap Sensitivity Analysis. The assembly of MEMS devices is challenging even when automated processes are used. The variation between devices can be large and so it is useful to investigate the effects of this. In the present device the tip gap is most likely to be affected although some nonalignment of the components is also possible. A tip gap sensitivity analysis at tip gaps of 5, 10, and 15 μm was performed using both the no-slip and slip-flow boundary conditions.

Figure 18 shows the variation in pressure ratio by decreasing the tip gap for the no-slip boundary condition. Superimposed are

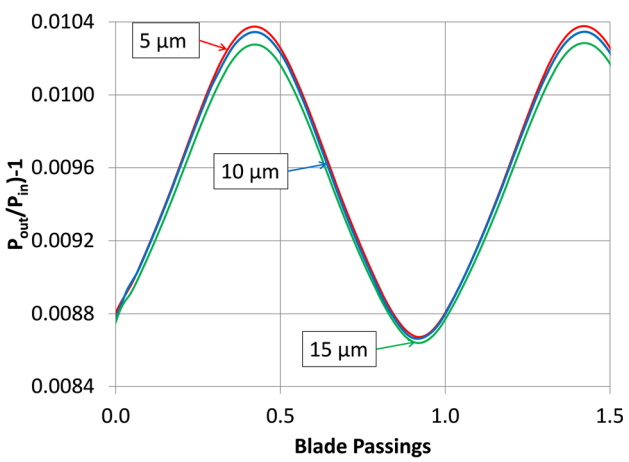

Fig. 19 Effect of tip gap on pressure ratio slip-flow

the variations for the slip-flow boundary conditions, which are expanded in Fig. 19. When no-slip boundary conditions are applied, the usual turbomachinery relationship of increasing pressure ratio with a decreasing tip gap occurs. However when slip-flow is applied this relationship is far weaker. In operation this would mean that the outer stages operating at higher pressure would be sensitive to the tip gap while the inner stages operating

at lower near vacuum pressure would not. Overall, it would still be desirable to have the tip gap be as small as possible.

Conclusion

The study shows that it is possible to model a roughing pump stage of a MEMS scale turbomachine using a commercial code. At Knudsen numbers below 0.1 the flow can still be treated as a continuum but requires the use of slip-flow boundary conditions. If accurate results are required, the wall shear must be specified based on the relationships of wall shear to the mean-free-path of the gas molecules. This method was validated against a classical solution of a pressure driven micro-Poiseuille flow. The specified-shear approach is computationally expensive while a good approximation of the flow can be obtained using a pure slip-flow boundary condition. This was shown to be true on 2D simulations of a generic roughing pump stage. The 2D simulations showed that at the near-zero flow rates found in a roughing pump the slip-flow boundaries gave higher pressure ratios than classical no-slip boundaries. Using the approximate slip-flow boundary conditions a 3D simulation of the stage was performed. Again the slip-flow boundary conditions resulted in a higher stage pressure rise. This suggests that the stages at the center of such a machine would operate with a higher pressure ratio than predicted using the classical no-slip boundary condition.

A tip gap sensitivity study showed that under no-slip boundary conditions, the pressure ratio of the stage is strongly dependent on the tip gap with reduced tip gaps, leading to higher pressure ratios. When the slip-flow boundary conditions are applied, the relationship is very small. It would still be desirable to have a small tip gap to ensure that the outer stages that are operating at higher pressures and thus with no-slip boundary conditions maximize their pressure ratios.

Acknowledgment

The authors would like to acknowledge the sponsorship of the Defense Advanced Research Projects Agency and thank the technical monitors Tayo Akinwande and Michael Wolfson.

Nomenclature

k = Boltzmann constant ($\mathrm{kg \cdot m^2/K \cdot s^2}$)
L = characteristic length scale (m)
$\mathcal{L}$ = mean-free-path (m)
p = pressure (Pa)
T = temperature (K)
u = velocity (m/s)
y = vector normal to wall

Greek Symbols

μ = viscosity ($\mathrm{Pa \cdot s}$)
ρ = density ($\mathrm{kg/m^3}$)
σ_c = molecular collision diameter (m)
σ_v = tangential-momentum-accommodation coefficient
τ = wall shear stress (Pa)

Subscripts

max = maximum velocity
ns = no-slip boundary
s = slip boundary
v = tangential slip velocity

References

[1] Lang, J. H., 2010, *Multi-Wafer Rotating MEMS Machines: Turbines, Generators, and Engines*, Springer-Verlag, New York.
[2] Rozanov, L. N., 2002, *Vacuum Technique*, CRC Press, Boca Raton, FL.
[3] Gad-el-Hak, M., 2002, *The MEMS Handbook*, CRC Press, Boca Raton, FL.
[4] Barber, R. W., and Emerson, D. R., 2002, "The Influence of Knudsen Number on the Hydrodynamic Development Length Within Parallel Plate Microchannels," *Advances in Fluid Mechanics*, Vol. IV, WIT Press, Southampton, UK, pp. 207–216.
[5] Basset, A. B., 1888, *A Treatise on Hydrodynamics*, Cambridge University Press, Cambridge, UK.
[6] Liou, W. W., and Fang, Y., 2006, *Microfluid Mechanics Principles and Modeling*, McGraw-Hill, New York.